PAPER

Check for updates

Elucidating the effect of mesopores on the conversion of green furans to aromatics over hierarchical Ga-MFI, Ga-MFI/MCM-41 composites, and Ga-SPP

Guido J. L. de Reijer, [a] Andreas Schaefer, [a] Anders Hellman [b] and Per-Anders Carlsson *[a]

Zeolitic catalysts used in the industrial manufacture of commodity chemicals excel thanks to their thermal stability, chemical tunability, and microporosity, aiding catalytic functions and shape- and size-selectivity that can be utilised also in reactions such as the conversion of biomass-derived furans into green aromatics, *i.e.*, benzene, toluene, and xylenes (BTX). However, excessive aromatization into polyaromatics and other carbonaceous species results in blocking of both active sites and micropores, ultimately deactivating the catalyst. As a solution, here, three classes of microporous materials comprising complementary meso- and/or macroporous domains have been synthesised and explored for the conversion of 2,5-dimethylfuran to BTX. First, meso- and macropores have been introduced in microporous Ga-MFI zeotype catalysts, with varying gallium content, *via* post-synthesis template-assisted base leaching. This increases the catalytic activity per acid site thanks to enhanced mass transfer properties, although at the expense of the acid site density, ultimately leading to similar overall production of aromatics. Second, gallium doped mesoporous silica, Ga-MCM-41, is shown to decrease the selectivity towards monoaromatics while increasing the formation of coke, due to the mere presence of mesopores. Through a one-pot, two-temperature step hydrothermal synthesis, Ga-MFI/MCM-41 composites were formed by partial transformation of the Ga-MCM-41 mesopore walls into microporous MFI-framework domains. Thereby, the selectivity towards benzene and isomerisation products increases while that for coke decreases. Third, Ga-containing self-pillared pentasil units (SPP) have been synthesised with varying gallium content. These materials possess both microporous MFI-domains and a broad size range of meso- and macropores in between said domains. However, due to its low acidity, almost no conversion of 2,5-dimethylfuran into benzene is observed. By comparing these three classes of materials, the critical role of the micropores is highlighted, as well as a potentially beneficial role of meso- and macropores. Moreover, the acid site density, generated by gallium, plays an important promoting role to convert 2,5-dimethylfuran into aromatics. Only when the majority of the material consists of microporous MFI, the selectivity is towards monocyclic aromatics such as benzene, instead of polycyclic aromatics and other coke species.

1 Introduction

The production of petrochemicals from fossil fuels relies on the use of catalysts, such as zeolites, to accelerate reactions, improve product selectivities and yields, and enable atom economic reactions, lowering energetic and monetary costs. Two-thirds of basic chemical production comprises commodity chemicals, such as the monocyclic aromatics benzene, toluene, and xylene (BTX),

which serve as building blocks for more than 90% of downstream organic chemical production.[1] A renewable and potentially sustainable alternative feedstock is lignocellulosic biomass, rich in aromatic components. Biomass can be converted into platform molecules such as furans through catalytic fast pyrolysis, producing, for example, 2,5-dimethylfuran (2,5-dmf), 2,5-dicarboxylic acid, furfural, and 5-hydroxymethylfurfural (HMF), which can be further converted into BTX.[2–7]

The use of zeolites as microporous solid acid catalysts for biomass conversion is advantageous not only because of their high surface area and thermal stability but also thanks to their tunable acidity and porosity aiding shape-selectivity. However, the zeolitic acid sites required for BTX production also catalyse the

[a] Department of Chemistry and Chemical Engineering, Chalmers University of Technology, SE-412 96 Gothenburg, Sweden. E-mail: per-anders.carlsson@chalmers. se; Tel: +46 (0)31 772 2924

[b] Department of Physics, Chalmers University of Technology, SE-412 96 Gothenburg, Sweden

This journal is © The Royal Society of Chemistry 2026

J. Mater. Chem. A, 2026, **14**, 12769–12784 | 12769

formation of polycyclic aromatics and hydrogen-deficient graphite-like hydrocarbons, ultimately deactivating the catalyst's functions. These carbonaceous species, referred to as coke, decrease catalyst efficiency in a few ways, *e.g.*, by inhibition of the active sites, blocking of micropores preventing access to the active sites, or even completely enveloping catalyst grains. To illustrate, the ZSM-5, which is a medium pore size zeolite comprising the MFI framework, is often used to catalyse the conversion of fossil fuels or biomass into aromatics.[8] Its two channels have maximum diameters of 5.5 and 5.6 Å at room temperature, which correspond to 6.2 and 6.3 Å at elevated reaction temperatures (500 °C) when applying Norman radii corrections that account for structural flexibility.[9,10] These dimensions are close to the kinetic diameters of reactants furan (5.1 Å), 2-methylfuran (5.3 Å) and 2,5-dmf (5.7 Å), as well as monoaromatic products benzene (5.85 Å), toluene (5.85 Å), and p-xylene (5.85 Å), driving selectivity towards desired BTX while suffering from deactivation when poly-aromatics are formed.[10–12]

Strategies to reduce the detrimental effects of coking include lowering the acidity of the catalyst, both the acid site density (here the number of acid sites per mass of catalyst is referred to as acid site density although not strictly a density) and the acid site strength of the catalyst. The density of acid sites can be reduced by dealumination,[13–15] while the substitution of framework Si and Al by boron, iron, or gallium reduces the strength of the Brønsted acid sites.[16,17] Recently, Sauer *et al.* showed that a gallium substituted, aluminium-free, MFI zeotype produces more BTX and has a longer lifetime in the catalytic conversion of 2,5-dmf into BTX than its aluminium containing ZSM-5 counterparts, clearly demonstrating the important effect of Ga on moderation of site acidity.[18] The effect of acid site density in Ga-MFI zeotypes was investigated by de Reijer *et al.* who compared a series of Ga-MFI zeotypes with varying gallium content. It was shown that a maximum production of benzene is achieved over catalysts with intermediate Ga content, *i.e.*, 6.7 and 8.6 wt% Ga for 1 and 3 h time-on-stream (TOS), respectively.[19] A further increase in the gallium content to 11 wt% was shown to shorten the lifetime of the catalyst due to rapid coking. Although the incorporation of gallium in the zeotype framework is promising for the valorisation of 2,5-dmf into BTX, previous works also show that BTX production per acid site decreases as the Ga content and acid site density increase, which suggests that many acid sites are not accessible in microporous Ga-MFI. Against this background, it is interesting to investigate ways to increase the access of 2,5-dmf to the Ga sites.

One approach to increase the reactant transfer rate to active sites in microporous materials is to create meso- (2–50 nm) or macropores (>50 nm) in addition to micropores (<2 nm). Fully mesoporous catalysts have been employed to valorise biomass-derived reactants, including the silica structures KIT-6, SBA-15, MCM-41, and MCM-48, doped with metals Al, Mg, Ti, Sn, Pt, Pd, Ru, Ga, W, Zr, Nb, La, Ce, or P.[20–29] Hierarchical zeolitic catalysts can also be used (for recent reviews see Mardiana *et al.*,[30] Li *et al.*,[31] Liu *et al.*[32] and Soltanian *et al.*[33]) For example, Kim *et al.* explored nanosponge-like beta zeolite for the Diels–Alder (D–A) cycloaddition of furans and alkenes to para-xylene.[34] Meso- and macropores can also be implemented in an existing microporous structure, for example, by dissolving part of the framework

in an alkaline solution, such as NaOH. This method targets inactive regions of the zeolite framework by preferentially dissolving Si–OH and Si–O–Si bonds, as opposed to M–O–Si (where M is the substituted metal), theoretically preserving the active acid sites. The extent of desilication, and thus framework dissolution, depends on several factors, such as the alkaline concentration, the nature of the base, the duration and temperature of the treatment, grain boundaries, structural defects, and the presence of protecting species. This method was used by, for example, Vasconcelos *et al.*[35] for furfural to isopropyl levulinate conversion and Pinard *et al.* for pyrolysis of biomass.[36]

Here, three different series of gallium-substituted MFI-based mesoporous zeolites were synthesised and studied in catalytic gas-phase conversion of 2,5-dmf into aromatics, each highlighting a different type of mesoporous material. By studying the structural similarities and differences and linking them to their catalytic performance, the role of mesopores can be elucidated. The first series consists of mesoporous Ga-MFI zeotypes, produced by subjecting microporous Ga-MFI, with a gallium content ranging from 1.2 to 11 wt%,[19] to a basic TPAOH solution. This dissolution–recrystallisation procedure introduced a secondary pore network of meso- and macropores. This series addresses the effect of introducing meso- and macropores through post-synthesis modification of a primarily microporous MFI precursor. The second series consists of Ga-containing MFI/MCM-41 composites, in which a mesoporous MCM-41 framework is first synthesised after which the outer surface of the mesopore walls is partially converted into microporous MFI, in a one-step hydrothermal crystallisation with two temperature steps. This series addresses the bottom-up approach of starting with a mesoporous framework and adding microporous regions inside, ensuring the presence of a well-ordered mesoporous network. The third series consists of Ga-containing disordered self-assembled pillared pentasil (Ga-SPP) units, which contain randomly ordered regions of microporous MFI, creating intercrystalline meso- and macropores.

The present objective is to compare how the synthesis method (top-down, bottom-up composite and self-assembly) for the creation of hierarchical Ga zeotypes comprising both micro- and mesoporosity affects the catalytic activity for the conversion of 2,5-dmf to aromatics. To this end, catalytic tests for the conversion of 2,5-dmf to aromatics were carried out using a fixed-bed chemical flow reactor with online Fourier transform infrared (FTIR) spectroscopy for continuous speciation of the product stream. Several techniques for the determination of catalyst morphology and physicochemical properties were used to characterise the effect of mesopore incorporation on the catalyst's gallium phase and the acidity resulting from the different synthesis routes, and to elucidate their effect on the target reaction.

2 Experimental

2.1 Catalyst materials

The catalysts studied in this work are synthesised bottom-up and divided into three classes, named after their gallium

12770 | *J. Mater. Chem. A*, 2026, **14**, 12769–12784

This journal is © The Royal Society of Chemistry 2026

content and micro- and mesoporous structure. Full synthesis details can be found in the SI.

The first class, named Ga-MFI$_{meso}$, is synthesised by post-synthesis dissolution and recrystallisation of a microporous parent Ga-MFI material,[19] employing a tetrapropylammonium hydroxide (TPAOH) solution.[37] The catalysts are named according to the gallium content of their parent material for clarity.

The second class, named Ga-MFI/MCM-41, is synthesised bottom-up through one-step hydrothermal crystallisation.[38] A low-temperature crystallisation first step (100 °C) promotes the formation of a mesoporous Ga-MCM-41 network while a consecutive high-temperature second step (160 °C) causes the partial transformation of MCM-41 into microporous MFI, resulting in hierarchical Ga-MFI/MCM-41 composites. For reference, a series of Ga-MCM-41 was synthesised as well by employing only the low-temperature crystallisaton first step.

The third class, named Ga-SPP, comprises gallium-containing self pillared pentasil units, in which slab-like MFI crystals bind orthogonally during the crystallisation process, resulting in disordered hierarchical morphology of microporous MFI domains.[39]

2.2 Characterisation of catalyst physicochemical properties

The elemental composition of the catalysts, for elements with an atomic number larger than eight, was determined by X-ray fluorescence spectrometry (XRF) using an AXIOS spectrometer (Malvern-Panalytical). Silicon and gallium were assumed to be in their oxide form and the water content was determined by thermogravimetric analysis.

The crystallinity of the catalysts was measured by powder X-ray diffraction (XRD) on a Bruker AXS D8 Discover diffractometer with monochromatic Cu-Kα radiation (1.5406 Å) from 2 to 50° 2θ.

Thermogravimetric analysis (TGA) coupled with differential scanning calorimetry (DSC) was carried out from 30 to 900 °C in 60 mL min^{-1} airflow using a Mettler Toledo TGA/DSC 3+ STARe system.

Textural properties of the catalysts were determined using N$_2$-physisorption at 77 K on a Micromeritics Tristar 3000 instrument after a pretreatment in N$_2$ at 250 °C for 16 h. The measurements were conducted using a filler rod as the focus is on mesopore analysis. Apparent surface areas were determined using the Brunauer–Emmett–Teller (BET) method[40] in the relative pressure range of $p/p_0 = 0.002$–0.03, according to the consistency criteria.[41] The microporous volume was determined by the t-plot method with the Harkins and Jura (HJ) equation,[42] using a thickness of $t = 5.0$–8.0 Å to minimize the underestimation caused by the curvature effect.[43] Pore size distributions (PSD) were derived from the adsorption isotherm using the Barrett–Joyner–Halenda (BJH) model.[44]

Morphological analysis was carried out using electron microscopy. Scanning electron microscopy (SEM) was performed on a Zeiss Ultra 55 FEG SEM with an accelerating voltage of 1.5 kV, as well as by energy-dispersive X-ray spectroscopy (EDX) on an FEI Quanta 200 FEG ESEM with an accelerating voltage of 20 kV. High-angle annular dark field scanning transmission electron microscopy (HAADF-STEM) was performed on a FEI Titan 80-300 TEM (300 kV).

The number of acid sites (acid site density) was analyzed by temperature-programmed desorption of ammonia (NH$_3$-TPD) in the catalytic reactor right before and directly after the catalytic tests, as well as after an oxidative calcination step after the reaction and after five cycles of reaction. Additional acid site analysis was performed with pyridine adsorption experiments using diffuse reflectance infrared Fourier transform spectroscopy (DRIFTS) on a Bruker VERTEX 70 spectrometer. Full details can be found in the SI.

2.3 Catalytic testing

Evaluation of the catalytic activity and selectivity of the zeotypes was carried out using a fixed-bed reactor. The effluent product mixture was analyzed online by Fourier-transform infrared spectroscopy (FTIR) on a gas analyzer (MKS MultiGas 2030). Products were quantified with the MKS software suite MG2000 v.10.2 and FTIR-library v.R3 by FTIR according to a method described in previous works.[45,46] Full details can be found in Table S1.

The liquid reactant 2,5-dmf was fed in low concentrations (300 to 720 ppm) to the reactor through a gas saturator and the reaction was performed at 500 °C for 1 or 3 h. The conditions were deliberately dilute to enable quantification of unconverted 2,5-dmf and reaction products with high time-resolution using FTIR spectroscopy.

For selected zeotypes, the stability of the catalysts was investigated by subjecting them to a total of five cycles of 3 h 2,5-dmf conversion at 500 °C, separated by 90 min oxidative regeneration in 20% O$_2$ at 600 °C (5 °C min^{-1}).

3 Results and discussion

This section starts with discussing the structural characterisation of the synthesised catalysts to establish a common ground for understanding the analysis of their catalytic performance in the conversion of 2,5-dmf.

3.1 Elemental composition

The effect of the introduction of meso- and macropores on Ga-MFI was explored through XRF spectrometry, as shown in Table S2. The atomic silicon-to-gallium ratios of zeotypes G1.2 and G3.1 decrease from Si/Ga = 95 and Si/Ga = 34 for microporous Ga-MFI to 81 and 27 for mesoporous G1.2 and G3.1, respectively, indicating a decrease in relative silicon content. This aligns with the understanding that a basic solution preferentially dissolves Si–OH, Si–O$^-$, and Si–O–Si bonds instead of Si–O–Ga, increasing the relative gallium content. However, for the zeotypes with a higher initial gallium content, the Si/Ga ratios increase, indicating a decrease in relative gallium content upon base treatment. This suggests that the gallium atoms present were not exclusively located in the framework, but also in the micropores as extra-framework gallium. Upon dissolution of their surrounding framework silicate species, the gallium species lose their anchoring sites or microporous confinement. It has been shown

by use of HAADF-STEM images that Ga-MFI$_{micro}$ catalysts with a gallium content of 6.0 wt% or higher may contain dispersed gallium-based nanoparticles, whose release here corresponds to the observed reduction in gallium content of Ga-MFI$_{meso}$. Full elemental compositions of Ga-MFI$_{meso}$ are shown in Table S2. Here, an increase in water content is observed when the gallium content increases along each series, which is ascribed to an increased affinity between water and Ga-based acid sites and/or cations. In addition, a potassium impurity is observed for all catalysts, originating from the KOH bath used to clean the Teflon® liners before synthesis.

3.2 Crystallinity and textural properties

The crystallinity of the catalysts was measured with X-ray diffraction and an overview is shown in Fig. 1, displaying the full diffractograms of Ga-MFI$_{meso}$ (panel a) and a close-up

(panel b), Ga-MCM-41 and Ga-MFI/MCM-41 (panel c), and Ga-SPP (panel d). Diffractograms of Ga-MFI$_{meso}$ display all peaks associated with the crystal lattice planes of the MFI framework structure, illustrated by the red bars.[47]

Comparing Ga-MFI$_{meso}$ (panel b, blue) to its parent material Ga-MFI$_{micro}$ (panel b, black), a clear resemblance in peak position, size, and shape can be observed. This indicates the preservation of the long-range crystalline structure. However, instead of one broad peak at 24.4° observed for G3.1$_{micro}$ and G6.0$_{micro}$, two peaks at 24.3 and 24.5° are observed for both G3.1$_{meso}$ and G6.0$_{meso}$. This indicates an increase in crystallinity, i.e., an increase in the degree of perfection of the framework lattice.[49]

Two explanations can be put forward for the observed increase in crystallinity: first, during the high-temperature step in basic TPAOH solution, crystallisation of amorphous fractions and/or recrystallisation of the partially dissolved framework can
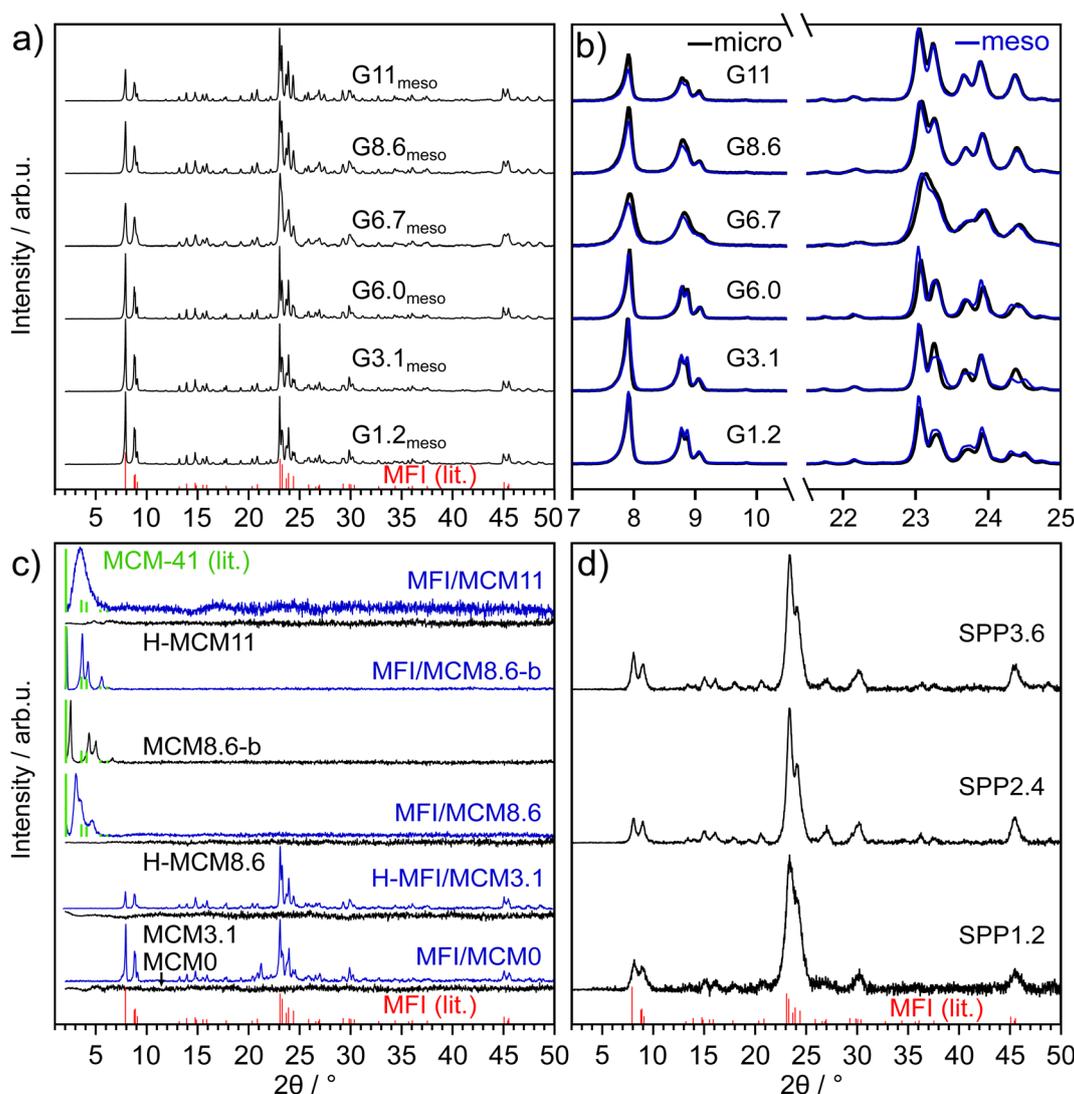

Fig. 1 XRD diffractograms of (a) Ga-MFI$_{meso}$ (b), a close-up of Ga-MFI$_{meso}$ (blue) and Ga-MFI$_{micro}$[19] (black), (c) Ga-MCM-41 (black) and Ga-MFI/MCM-41 composites (blue), and (d) Ga-SPP catalysts. Catalysts in panel (c) are in their final protic form (indicated by 'H−') or in their calcined Na-form. All diffractograms are normalized to their most intense peak except for Ga-MCM-41, as no peaks were distinguished. Peaks associated with the crystal lattice planes of the MFI framework structure[47] and MCM-41 structure[48] are denoted by red and green bars, respectively.

12772 | J. Mater. Chem. A, 2026, **14**, 12769–12784

This journal is © The Royal Society of Chemistry 2026

take place, increasing the overall crystallinity.[37] This effect preferentially takes place at lattice imperfections, or defect sites, essentially 'healing' the zeotype lattice. Examples of such defects in MFI zeotypes are isolated internal and external silanol (Si–OH) groups, nonbridging oxygen atoms ($=$Si–O$-$), or a missing tetrahedral (T) framework atom, which results in a group of four Si–OH groups called a silanol nest. Second, and in line with the first explanation, the dissolved and released Ga species migrate throughout the sample and reattach to, or nestle into, the zeotype surface, preferentially on defect sites.

In panel c, no peaks are observed for any of the Ga-MCM-41 materials besides MCM8.6-b (black), indicating the absence of a well-ordered long-range crystalline meso- or microporous structure. However, when only a small quantity of material is produced and measured, a much smaller volume is probed by X-rays and thus the intensity of the diffracted X-rays and signal-to-noise ratio (SNR) will be much lower, rendering peak identification challenging. This suggests that the absence of peaks does not fully exclude the presence of a mesoporous structure. After the second crystallisation step at higher temperatures, Ga-MCM-41 transforms into MFI/MCM-41 composites (c, blue). For lower gallium contents, 0 and 3.1 wt%, a complete or partial transformation is confirmed by the presence of the peaks characteristic of the MFI structure (red bars). For MFI/MCM8.6, several broad peaks are observed in the mesoporous regime while only one broad peak is observed for MFI/MCM11. This indicates an increase in the fraction of ordered mesoporous material compared to its Ga-MCM-41 analog, although no transformation into MFI is observed.

To attempt to synthesise Ga-MFI/MCM-41 composites with high Ga content, a total of 24 materials were prepared to investigate the influence of the base concentration, the alkali source, and the ageing conditions. An overview of the precursor gel compositions is shown in Table S3, the XRD diffractograms in Fig. S1, and a description of the synthetic study is provided in the SI. In short, highly crystalline Ga-MCM-41 with a target gallium content of 8.6 wt% was synthesised by employing longer ageing times in acidic medium, as well as an increased NaOH concentration; denoted as MCM8.6-b in Fig. 1. After the second crystallisation step, producing MFI/MCM8.6-b, the peaks shift to lower angles of 2.2, 3.7, 4.2, and 5.6°, aligning with the reflections of an Al-MCM-41 reference (green bars).[48] The peak shift indicates an increase in d-spacing and thus an increase in the average mesopore size, which is in line with physisorption results discussed in detail below. It is proposed that this results from the partial dissolution of the inner wall of the mesopores of MCM8.6-b, which was formed in the first low-temperature crystallisation step. Consecutive recrystallisation of the dissolved species into MFI was not observed, possibly due to an unfavourable pH. The one-pot synthesis of Ga-MFI/MCM-41 composites with high gallium loadings ($\geq$8.6 wt%) has proven to be challenging and the materials presented in Fig. 1 were selected for further structural analysis and catalytic testing. Please note, for clarity, the samples exposed to both crystallisation steps are still referred to by 'MFI/MCM', although the presence of an MFI phase has not been confirmed for high gallium contents.

The diffractograms of the Ga-SPP series (panel d) contain broad peaks associated with the MFI framework. The
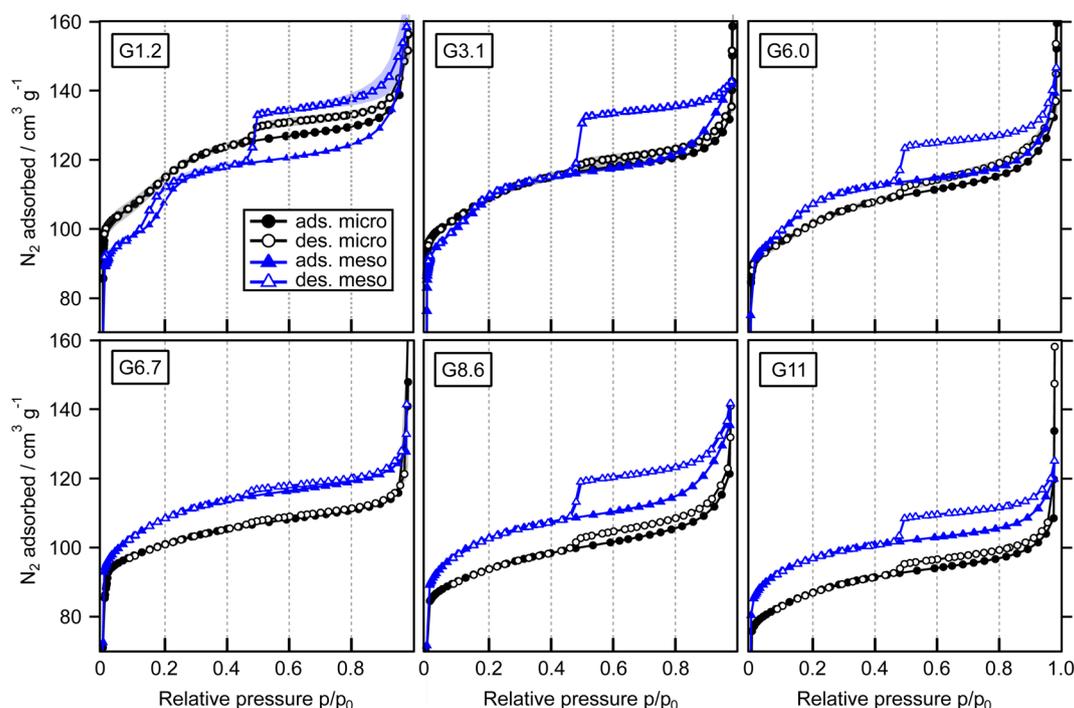

Fig. 2 N$_2$-physisorption isotherms of the Ga–MFI$_{micro}$ (black circles) and Ga–MFI$_{meso}$ (blue triangles) including adsorption (filled) and desorption (empty). The numbers denote the gallium content of the microporous parent material. The measurement was repeated for microporous G1.2, G3.1, G6.0, G6.7, and mesoporous G1.2 and an average curve is shown, as well as the variance indicated by the shaded area.
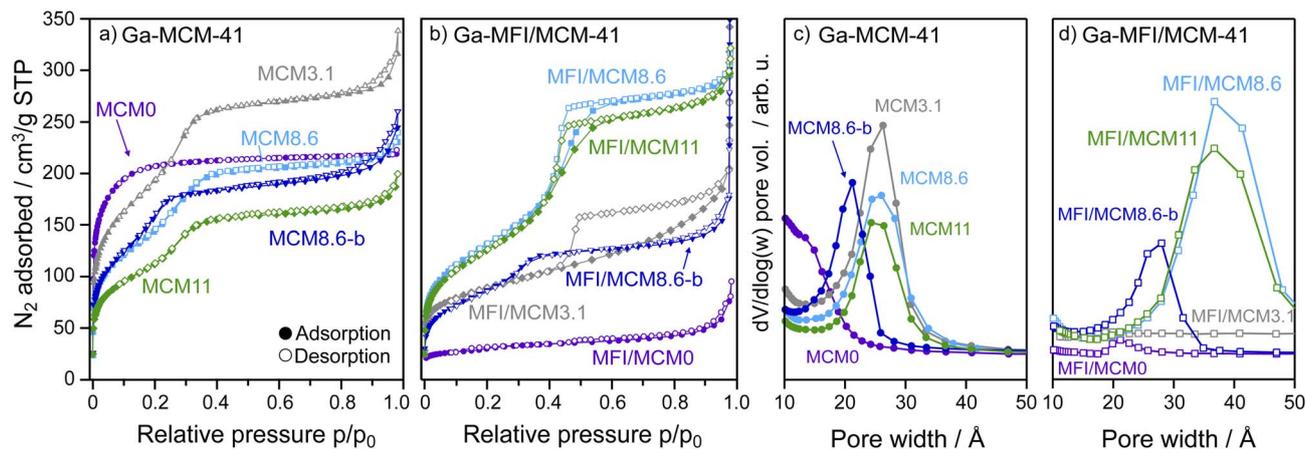
This journal is © The Royal Society of Chemistry 2026

J. Mater. Chem. A, 2026, **14**, 12769–12784 | **12773**

Fig. 3 N_2-physisorption isotherms of (a) Ga-MCM-41 and (b) Ga-MFI/MCM-41. Apparent pore size distributions determined applying the BJH-model to the adsorption curve for (c) Ga-MCM-41 and (d) Ga-MFI/MCM-41.

broadening and overlap of the peaks indicate a variation in the crystal lattice parameter. This can be explained by the random ordering of pentasil units during the formation of SPP. The SNR of SPP2.4 is higher than both SPP3.6 and SPP1.2, suggesting that a moderate amount of acidic gallium precursors resulted in the optimal pH for hydrolysis, condensation, and crystallisation, as the amount of added TBAOH was constant.

The porosity of the catalysts was investigated with nitrogen physisorption. The isotherms of Ga-MFI$_{meso}$ and Ga-MFI$_{micro}$ are shown in Fig. 2, of Ga-MCM-41 and Ga-MFI/MCM-41 in Fig. 3, and of Ga-SPP in Fig. 4. The corresponding pore size distributions (PSD) are shown in Fig. S2, 3c, d, and 4 insert, respectively. The determined surface areas as well as the microporous and mesoporous volumes are shown in Table 1.

Starting with the isotherms of Ga-MFI$_{meso}$ (blue curves), their shapes appear as composites of type I and type IV, characteristic of microporous and mesoporous materials, respectively.[50] The steep nitrogen uptake at the lowest relative pressures (not displayed in detail here) corresponds to the nitrogen filling of micropores. With

increased relative pressure, a step/curvature is observed at relative pressures below 0.2, which is due to a phase transition of the adsorbate.[51] For the mesoporous G1.2 sample also a hysteresis is observed in this region, which will be discussed in more detail below. With an even further increase in relative pressure, the nitrogen uptake increases gradually due to filling of mesopores. The observed hysteresis loop between $p/p_0 = 0.42$–0.98 for all samples, classified as type H4, is due to capillary condensation in the mesopores during the adsorption. The forced closure of the desorption and adsorption curves at $p/p_0 = 0.42$ is the result of the so-called tensile strength effect.[51] In most cases, the general shapes of the isotherms for the Ga-MFI$_{meso}$ catalysts are similar to the corresponding curves (black) for the Ga-MFI$_{micro}$ catalysts. However, the area enclosed in the hysteresis loop is larger for the Ga-MFI$_{meso}$ catalysts as compared to their microporous counterparts, which is indicative of a larger total mesoporous volume. The hysteresis seen for the Ga-MFI$_{micro}$ catalysts is suggested to originate from mesoporosity between crystallites.[19,50] In this regard, the G6.7$_{meso}$ and G6.7$_{micro}$ samples stand out showing very small hystereses. This is likely due to the much smaller crystallites for the parent microporous material limiting both inter-crystallite voids and intra-crystallite pores (as dissolution of large volumes of material in small crystallites is not possible) to contribute to mesoporosity. For G1.2$_{meso}$ and G3.1$_{meso}$, the amount of nitrogen adsorbed after filling of the micropores at low pressures (microporous volume) as well as the microporous surface area, is lower than its microporous counterpart. This follows from the partial dissolution of the microporous regions during the synthesis of Ga-MFI$_{meso}$, creating mesopores. However, for catalysts with a higher gallium content, the microporous volume remains equal (G6.0$_{meso}$) or increases upon mesopore introduction (Table 1). This can be explained by the following three phenomena. First, the gallium content of these zeotypes decreases upon mesopore introduction, as was shown by XRF, likely due to the removal of gallium-based nanoparticles present as extra-framework species. These nanoparticles are several nanometres in diameter and thus prevent nitrogen molecules from entering the micropores of Ga-MFI$_{micro}$ during nitrogen physisorption measurements,
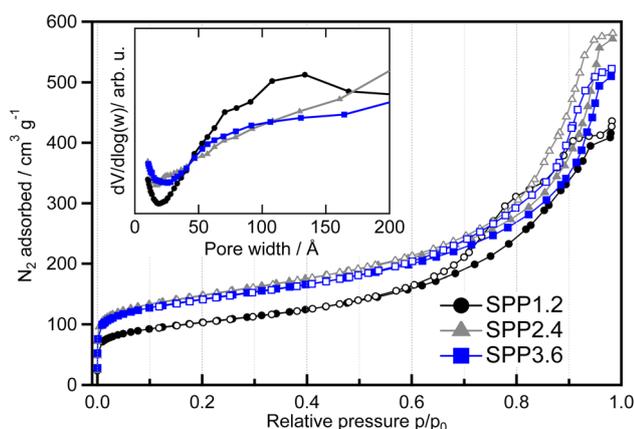

Fig. 4 N_2-physisorption isotherms of Ga-SPP, including SPP1.2 (black circles), SPP2.4 (grey triangles), and SPP3.6 (blue squares). The inset displays the PSD determined by applying the BJH-model to the adsorption curve.

12774 | *J. Mater. Chem. A*, 2026, **14**, 12769–12784

This journal is © The Royal Society of Chemistry 2026

Table 1 Physicochemical properties of Ga-MFI$_{meso}$, Ga-MCM-41, Ga-MFI/MCM-41, and Ga-SPP

Sample	S. A.[a] (m^2 g^{-1})	V_{micro}[b] (cm^3 g^{-1})	S_{ext}[c] (m^2 g^{-1})	Acidity[d] (mmol g^{-1})
Ga-MFI$_{meso}$				
G1.2$_{meso}$	398	0.166	28	0.052
G3.1$_{meso}$	401	0.164	25	0.124
G6.0$_{meso}$	395	0.161	22	0.140
G6.7$_{meso}$	416	0.161	26	0.249
G8.6$_{meso}$	393	0.150	28	0.212
G11$_{meso}$	374	0.144	21	0.354
Ga-MCM-41				
MCM0	1503	0.685	66	N.A.[e]
MCM3.1	1173	0.902	115	0.265
MCM8.6	814	0.609	55	0.280
MCM8.6-b	558	0.261	44	0.382
MCM11	661	0.485	56	0.161
Ga-MFI/MCM-41				
MFI/MCM0	105	0.038	26	N.A.
MFI/MCM3.1	317	0.085	140	0.309
MFI/MCM8.6	499	0.378	51	0.285
MFI/MCM8.6-b	327	0.168	37	0.327
MFI/MCM11	474	0.342	66	0.313
Ga-SPP				
SPP1.2	369	0.014	314	0.001[e]
SPP2.4	532	0.093	314	0.003[e]
SPP3.6	508	0.084	305	0.007[e]

[a] Apparent surface area determined by N$_2$-physisorption and BET method[40] ($p/p_0 = 0.002$–0.03 following consistency criteria[41]). [b] Microporous volume as determined *via* t-plot method[42] (Harkins and Jura equation, $t = 6.0$–9.0 Å for Ga-MCM and $t = 5.0$–8.0 Å for other catalysts). [c] External surface area of mesoporous Ga-MFI zeotypes. Determined by t-plot method[42] (Harkins and Jura equation, $t = 6.0$–9.0 Å for Ga-MCM-41 and $t = 5.0$–8.0 Å for other catalysts). [d] Acid site density determined by NH$_3$-TPD to 600 °C. [e] Low reliability due to low SNR of ammonia concentration.

underestimating the actual microporous area and volume of the parent material. Consequently, the improved access to the microporous regions in Ga-MFI$_{meso}$ may give the illusion of an increase in microporous MFI fraction. Second, during dissolution in alkaline solution, framework gallium acts as a protecting species and Si–O–Si bonds are preferentially dissolved. For high gallium content zeotypes, with more framework Ga, dissolution of microporous regions into mesopores happens to a lower degree. This is supported by the smaller size of the hysteresis loop of Ga-MFI$_{meso}$ (Ga wt% ≥6.0) compared to G1.2$_{meso}$ and G3.1$_{meso}$. Third, the presence of the template TPA$^+$ results in the recrystallisation of dissolved nutrients into microporous MFI.

Although no hysteresis is expected for p/p_0 below 0.42 when nitrogen is used as adsorptive, the isotherm of G1.2$_{meso}$ clearly contains a hysteresis accompanying the step below $p/p_0 = 0.2$. Llewellyn *et al.* showed by use of sorption, microcalorimetry and neutron diffraction, that adsorption of nitrogen onto zeolite surfaces has a certain site dependence and that the structure of adsorbed nitrogen molecules can change between a disordered fluid-like phase and a crystalline-like solid phase.[52] Here, this hysteresis is likely due a transition from the disordered fluid-like phase to the crystalline solid phase, which has been observed in other studies[53–56] and is similar to the behaviour of G0$_{micro}$ (silicalite-1) and G0.5$_{micro}$ in previous work.[19] Although one cannot unambiguously state whether or not this

phenomenon depends on the gallium or acid site density, it seems to correlate with the latter; G1.2$_{meso}$ has lost more than half of its acid site density from 0.119 for G1.2$_{micro}$ to 0.052 mmol g^{-1}, while G1.2$_{micro}$ does not display this hysteresis behaviour.

Analysis of sorption data is often considered a quick approach to understand porosity in more detail including, for example, pore size distributions (PSD). However, extracting PSDs from isotherms needs to be done carefully. The analysis of the adsorption curve is preferred over the desorption curve because (i) using the desorption curve, that closes at 0.42 independent of sample, would lead to an erroneous pore size at around 38 Å that stem from the tensile strength effect rather than a real pore and (ii) real samples often include a porous network rather than cylindrical pores affecting the isotherms.[51] Here, using the adsorption isotherm, diameters in the range 13 to 19 Å are observed for both the micro- and mesoporous catalysts, see Fig. S2. The pore sizes for the latter type are somewhat smaller. However, one cannot unambiguously state whether or not these are real because they stem from the isotherm curvature at relative pressure around 0.2, for which the nitrogen phase transition occurs. Further, one may find the smaller size for the mesoporous samples as compared their microporous counterparts contradictory to the fact that the mesoporous samples show a much more pronounced hysteresis

This journal is © The Royal Society of Chemistry 2026

J. Mater. Chem. A, 2026, **14**, 12769–12784 | **12775**

indicative of larger mesoporous volume as discussed above. Thus, it is likely that adsorbate phase transition is the cause for these pore sizes. Interestingly, there seems to be a trend for the mesoporous samples showing a decreasing pore size as a function of increased gallium content, which may suggest that the gallium interacts with the nitrogen, in a similar way as nitrogen molecules may experience quadrupole–quadrupole interactions, influencing the phase transition. This would be in line with TGA analysis showing an increased water content with increasing gallium content, i.e., the more gallium, the more interactions with adsorptives. Further, pore sizes in the range 20 to 30 nm are observed for most of the mesoporous samples, which is in line with their hystereses. These pores are considered real and are supported by the electron microscopy imaging discussed below. Again, the G6.7 sample shows no clear mesopores in line with the small hysteresis discussed above and electron microscopy imaging discussed below.

The nitrogen physisorption isotherms and PSD of Ga-MCM-41 and Ga-MFI/MCM-41 are shown in Fig. 3. The isotherm of MCM0 resembles reversible type I(b), belonging to materials with a narrow distribution of large micropores or narrow mesopores of <25 Å.[50] This is confirmed by the PSD (panel c), suggesting a peak below 10 Å. The isotherms of MCM3.1, MCM8.6, and MCM11 are of reversible type IV(b), associated to mesoporous adsorbents. The pronounced adsorption step between $p/p_0 = 0.3$–0.4 is caused by capillary condensation and its position is related to the pore width; an inflection point at higher pressures for MCM3.1 corresponds to a larger pore diameter.[44,57] Moreover, the lack of hysteresis indicates that the mesopores are smaller than the critical diameter of approximately 40 Å for nitrogen at 77 K.[58] This is confirmed by the PSD giving 31, 28, and 26 Å as the pore diameter for MCM3.1, MCM8.6, and MCM11, respectively.

The nitrogen physisorption isotherms and PSD of Ga-SPP are shown in Fig. 4. The isotherms are composites of reversible type II and type IV, associated to macroporous and mesoporous adsorbents, respectively.[50] The absence of a steep adsorption step like observed for Ga-MCM-41 indicates the lack of well-ordered mesopores with a narrow PSD. Hysteresis loops of type H3 are observed between $p/p_0 = 0.6$–0.98 for all three gallium loadings, which typically indicate the incomplete filling of meso- and macropores. The PSD suggests the presence of a microporous fraction ≤10 Å that fills up at a pressure below $p/p_0 = 0.1$, although this might be the formation of a monolayer as was seen for Ga-MCM-41. Additionally, all Ga-SPP samples display a broad size distribution of pore widths ≥50 Å, confirming the disordered random pore structure of the Ga-SPP catalysts.

The textural properties of Ga-MCM-41 and Ga-SPP are shown in Table 1. The total apparent surface areas determined using the BET method range from 1503 m^2 g^{-1} for MCM0 down to 661 m^2 g^{-1} for MCM11, while the microporous volume ranges from 0.902 cm^3 g^{-1} for MCM3.1 to 0.485 cm^3 g^{-1} for MCM11. However, for the t-plot method, the thickness layer from 6.0 to 9.0 Å was selected to include the filling of the mesopores at $p/p_0 = 0.3$, translating the determined microporous volume into mesoporous volume.

For the Ga-SPP samples, the surface area and microporous volume decrease in the order of SPP2.4 > rbin SPP3.6 > rbin SPP1.2 from 532, 508, and 369 m^2 g^{-1}, and 0.093, 0.084, and 0.014 cm^3 g^{-1}, respectively. This confirms the results from XRD based on the SNR; i.e., that the fewest ordered microporous MFI regions were formed for SPP1.2, followed by SPP3.6 and SPP2.4. The high external surface area of more than 300 m^2 g^{-1} determined for each Ga-SPP, demonstrates the presence of meso- and macropores.

3.3 Morphology

The SEM images of Ga-MFI$_{meso}$ are shown in Fig. S3, demonstrating the presence of large aggregates of crystallites for all zeotypes, similar to their microporous parent material Ga-MFI$_{micro}$.[19] Most zeotypes possess a heterogeneous size- and shape distribution, although an additional layer of crystalline material has formed on the outer layer of crystal aggregates for G6.0$_{meso}$, G6.7$_{meso}$, G8.6$_{meso}$, and G11$_{meso}$. This is caused by the recrystallisation of dissolved material in the presence of TPAOH, which can also lead to the creation of fissures and macropores as was observed for G8.6$_{meso}$.

HAADF-STEM images of Ga-MFI$_{meso}$ are shown in Fig. 5, demonstrating the successful introduction of meso- and macropores inside crystal aggregates. The mesopores, represented by black spots (absence of material), are present in a range of sizes, e.g., 20 × 20 nm, 50 × 50 nm, or larger as observed in G3.1$_{meso}$ and G6.0$_{meso}$ (macropores). For low gallium content zeotypes, G1.2$_{meso}$ and G3.1$_{meso}$, most mesopores are empty, although some agglomerates are visible in G3.1$_{meso}$, ascribed to gallium-based nanoparticles. These nanoparticles are also observed in G6.0$_{meso}$, G8.6$_{meso}$, and G11$_{meso}$, and are formed when framework Si–O–Si dissolves; releasing framework Ga as well as anchored extra-framework Ga-species, which agglomerate and are trapped inside the meso- and macropores. No mesopores and gallium-based nanoparticles were observed for G6.7$_{meso}$, again, likely owing to its small crystal size of 500 to 1000 nm, preventing the leaching of OH$^-$ deep inside the crystal aggregates. The TPA$^+$ molecules are too large to enter the micropores and thus reside on the external surface of the crystals and prevent them from dissolving. As follows from the small crystal size, their high surface-to-volume ratio increases the number of protecting groups and thus reduces the extent of dissolution by OH$^-$. Again, this is also supported by the small hysteresis loop of G6.7$_{meso}$ caused by mesopores. To identify the chemical character of the debris of material in the mesopores, HAADF-STEM EDX was measured on G8.6$_{meso}$, as shown in Fig. S4. Here, bright clusters are confirmed to be gallium-based, presumably in oxide form as no metallic gallium could be detected with X-ray photoemission spectroscopy (not shown).

SEM images of Ga-MCM-41 and Ga-MFI/MCM-41 composites are shown in Fig. S5. Here, MCM0 consists of agglomerates of smooth crystals of inconsistent shape and size. After the additional high-temperature crystallisation step, MFI/MCM0 comprises lamellar, petal-like, coffin-shaped, and needle-shaped crystals. The needles and coffin-shaped crystals are typical
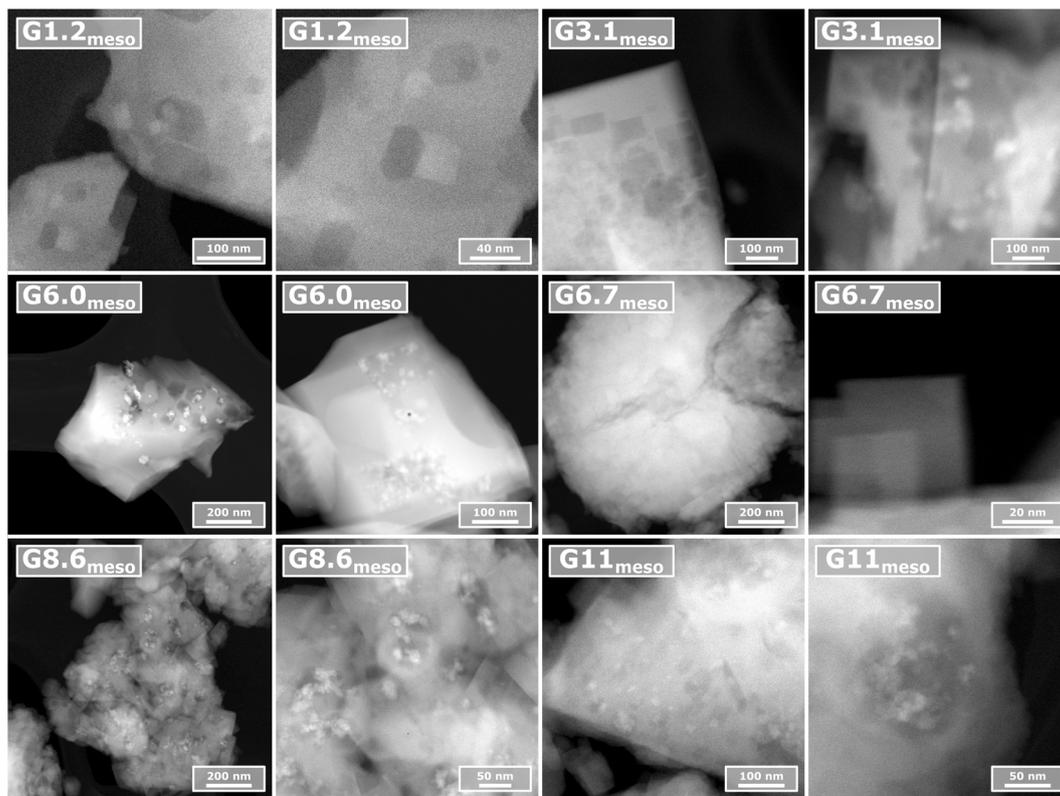
12776 | J. Mater. Chem. A, 2026, 14, 12769–12784

This journal is © The Royal Society of Chemistry 2026

Fig. 5 HAADF-STEM images of Ga-MFI$_{meso}$ zeotypes recorded at 300 kV.

for MFI materials,[59] whereas the lamellar structure may possibly be ascribed to MCM-41 material. MCM3.1, with crystal aggregates consisting of randomly shaped and oriented crystallites, partially transforms into spherical rods with a diameter of between 5 and 10 μm. MCM8.6, MCM11, MFI/MCM8.6, and MFI/MCM11 consist of crystal agglomerates of varying size, each comprising randomly sized- and shaped smaller crystallites. TEM images of MCM3.1 (Fig. S6) show the presence of lattice fringes while HAADF-STEM shows that both MCM3.1 and MFI/MCM3.1 are made up of randomly oriented needles and plates.

The morphological features of Ga-SPP were also investigated with SEM, TEM, and HAADF-STEM, and an overview is shown in Fig. S7. All three catalysts consist of large crystal aggregates possessing lamellar structures and accomodating large pores of up to 1 micrometer in diameter. With TEM, microstructured regions are identified in SPP3.6 (panel F), as illustrated by lattices fringes. These crystals are up to 25 micrometers in length, suggesting the random orientation of the pentasil units comprising the MFI structure.

3.4 Acid site density, strength and speciation

The acid site density and acid site strength were determined with NH$_3$-TPD, while the types of acid sites in Ga-MFI$_{meso}$ and Ga-MFI$_{micro}$ were further studied with pyridine DRIFTS.

Fig. 6 shows the NH$_3$-TPD spectra of the fresh Ga-MFI$_{meso}$ (light blue) and parent Ga-MFI$_{micro}$ (green) catalysts for each gallium content. Additionally, the figure includes pie charts that

show the distribution of the acid sites probed by pyridine DRIFTS classified into strong Brønsted acid sites (sBAS, green), weak Brønsted acid sites (wBAS, orange), strong Lewis acid sites (sLAS, dark blue) and weak Lewis acid sites (wLAS, light blue). For all MFI zeotypes, acid sites are lost during the introduction of the mesopores, in particular strong and extra strong acid sites, as determined by the desorption of ammonia at temperatures above 250 °C. The acid site densities are quantified, as shown in Tables 1 and S4, and 44, 46, 55, 59, 49, and 58% of acid sites remain after mesopore introduction for G1.2$_{meso}$, G3.1$_{meso}$, G6.0$_{meso}$, G6.7$_{meso}$, G8.6$_{meso}$, and G11$_{meso}$, respectively. This reduction of roughly half of the number of acid sites suggests that the 0.2 mol L^{-1} TPAOH treatment at 170 °C in an autoclave for 24 h is too harsh and results in too extensive dissolution of the acid sites and/or the chemical environment of the active site. Along the Ga-MFI$_{meso}$ series, an increase in gallium content corresponds to an increase in acid site density, with the exception of G8.6$_{meso}$ (0.212 mmol g^{-1}). Its relatively low acid site density displays the varying effects of TPAOH treatment on the catalysts, which is suggested to be caused by the heterogeneity of the microporous parent material.

To elaborate on the lost acid sites, as determined by pyridine DRIFTS (Fig. S8), the fraction of sBAS reduces for all MFI zeotypes while a reduction in sLAS is also observed in G1.2$_{meso}$ and G6.0$_{meso}$. We mention that the distribution is based on a normalised sum of all acid sites to 100% and as such an apparent increase in an acid site fraction may still correspond to a decrease in the absolute number, i.e., acid site density, of that type of acid site. Remarkably, the NH$_3$-TPD for G6.0$_{meso}$ shows
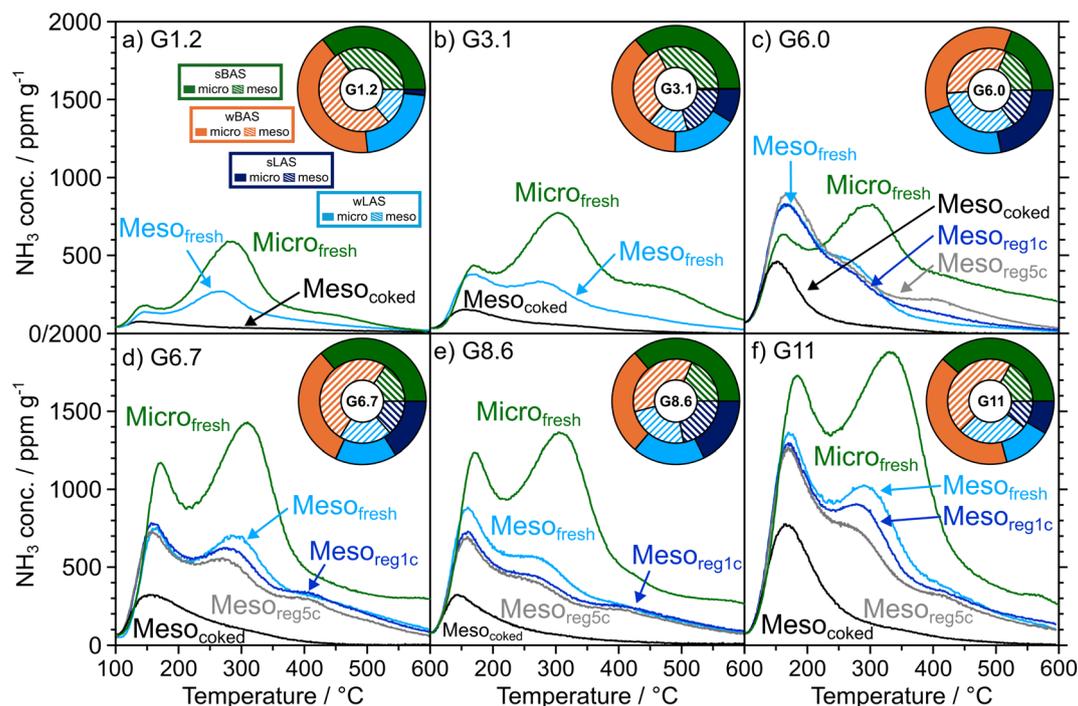
This journal is © The Royal Society of Chemistry 2026

J. Mater. Chem. A, 2026, 14, 12769–12784 | 12777

Fig. 6 Characterisation of acidity of the (a) G1.2, (b) G3.1, (c) G6.0, (d) G6.7, (e) G8.6 and (f) G11 catalysts. NH_3-TPD profiles of fresh Ga–MFI$_{micro}$ (green)[19] mesoporous (blue), coked after 3 h reaction (black), regenerated after first cycle (index 1c, dark blue), regenerated after five cycles of 3 h reaction (index 5c, grey).The acid site distribution is displayed for fresh micro- (filled) and meso- (patterned) Ga-MFI zeotype, with strong BAS (green), weak BAS (orange), strong LAS (dark blue), and weak LAS (light blue).

an increase in acid sites, namely weak acid sites with desorption temperatures below 200 °C. These sites were generated during TPAOH treatment, and is suggested to originate from the mobilization of framework and non-framework gallium species. These may originally be acidic or non-acidic in nature, and may be relocated upon dissolution of framework material in OH^-. Using pyridine DRIFTS, these sites can be classified as weak Lewis acid sites, as their wLAS fraction (light blue) increases.

Furthermore, NH_3-TPD was performed directly after 2,5-dmf conversion reaction in coked state (black), after oxidative regeneration (dark blue), and after four more cycles of reaction and oxidative regeneration (grey). These results are discussed below in connection to the catalytic tests.

The acidity of Ga-MCM-41 and Ga-MFI/MCM-41 composites were studied with NH_3-TPD, as shown in Fig. 7 and S9. For all
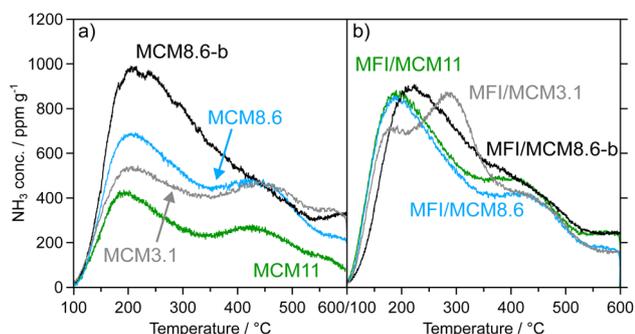
samples, several peaks were observed, classified as weak acid sites ($T_{desorption} < 200$ °C), strong acid sites ($250 \leq T_{desorption} \leq 350$ °C), and extra strong sites ($T_{desorption} > $ rbin 350 °C). The TPD profiles were quantified and the acid site densities are shown in Table 1, ranging from 0.161 mmol g^{-1} for MCM11 to 0.349 mmol g^{-1} for MCM8.6-b. After the additional high temperature crystallisation, the acid site density was increased for most catalysts, in particular the weak and medium ($200 \leq T_{desorption} \leq 250$ °C) strength acid sites. For MFI/MCM3.1, a large peak around 290 °C appeared, suggesting that this acid site derives from gallium in the MFI structure.

Ga-SPP catalysts were also evaluated by NH_3-TPD. Their acid site densities are very low, with 0.001, 0.003, and 0.007 mmol g^{-1} for SPP1.2, SPP2.4, and SPP3.6, respectively. Perhaps the incorporation of gallium into the framework of the catalysts requires a well-ordered assembly of the pentasil units into chains, sheets, and subsequently a three-dimensional structure with micropores. The randomly oriented self-assembly of the Ga-SPP pentasil units may exclude the formation of acid sites. The exact nature of the gallium present remains unknown, as no gallium-based nanoparticles were detected with electron microscopy.

3.5 Catalytic activity and selectivity

To test catalytic performance, each catalyst was exposed to dilute 2,5-dmf in argon for 3 h at 500 °C while the main gas products were quantified using on-line FTIR spectroscopy.[45,46] From that, the conversions and selectivities (excluding coke)

Fig. 7 NH_3-TPD profiles of (a) Ga-MCM-41 and (b) Ga-MFI/MCM-41.

12778 | *J. Mater. Chem. A*, 2026, **14**, 12769–12784

This journal is © The Royal Society of Chemistry 2026

were calculated using eqn (1) and (2) described in the SI. The coke selectivity was determined after catalytic tests by the amount of carbon removed as CO and CO_2 during oxidative regeneration.

Starting with the Ga-MFI$_{meso}$ and Ga-MFI$_{micro}$ catalysts, an overview of the formed benzene is shown in Fig. 8. For all Ga-MFI$_{meso}$ catalysts, the initial conversion of 2,5-dmf exceeds 85% and for a few it is nearly 100% with BTX selectivity in the range 60 to 82%. The carbon balance is high, in the range 87–98% (see Table 2 for a summary of all conversions, BTX and coke selectivity and carbon balance). This is higher than for their Ga-MFI$_{micro}$ counterparts. Compared to previous work, it is higher than for ZSM-5 showing 64% conversion with 42.6% selectivity to aromatics[60] at 600 °C as well as Ga/HZSM-5 prepared by incipient wetness impregnation, for which the selectivity towards BTX was reported to be ca 45% (although initial conversion was 100%).[61] As can be seen, the formation of benzene decreases as a function of time on stream. It decreases more rapidly for the Ga-MFI$_{meso}$ catalysts than for the Ga-MFI$_{micro}$ catalysts. The decrease in benzene formation can be better understood by looking at Fig. 9, which shows the 2,5-dmf conversion and the selectivity to benzene as well as other products for the Ga-MFI$_{meso}$ catalysts over three hours. It is clear that, as a function of time-on-stream, the 2,5-dmf conversion continuously declines while the overall selectivity

Fig. 8 Benzene production over the first 60 min TOS of (a) Ga-MFI$_{meso}$ zeotypes and (b) Ga-MFI$_{micro}$ parent material. The catalysts are named according to the gallium content of the parent material, including G1.2 (maroon), G3.1 (grey), G6.0 (black), G6.7 (blue), G8.6 (green), and G11 (purple).

changes. After about 30 min, formation of products such as indene, 2,4-dimethylfuran (2,4-dmf), 2-methylcyclopentenone (2-mcpo), 3-methylcyclopentenone (3-mcpo), and 2-methylfuran, start at the expense of benzene formation. Toluene is produced with a low selectivity, reaching a maximum of 6.9% over G3.1$_{meso}$, while xylenes are not detected.

The aromatisation is generally considered to proceed via a Diels–Alder (D–A) reaction mechanism, which needs a diene to react with the 2,5-dmf.[5] Here 2,5-dmf is suggested to crack due to ring-opening over sBAS creating an olefin pool that supplies dienes to the D–A reaction. The desired monocyclic aromatics are then formed over sBAS and sLAS. We mention that co-feeding of olefines increase the yield of monocyclic aromatics at temperatures above 500 °C (not shown). The selectivity change is likely caused by the formation of carbon deposits known as coke, comprising aliphatics, polyaromatic hydrocarbons, and graphite,[62] deactivating certain catalytic functions (sites). The coke can be considered as hard coke as it is formed at 500 °C. Further, as catalyst regeneration by oxidation with 20% O_2 required elevated temperature, i.e., 600 °C, the coke is likely dominated by graphite-like carbon for both micro- and mesoporous samples.[63] After three hours of TOS, the main product is the 2,4-dmf isomer, reaching 58.9% selectivity over G1.2$_{meso}$ at 35.0% conversion. The isomerisation of 2,5-dmf into 2,4-dmf is considered to occur through acid-catalysed methyl-migration, facilitated by steric confinement in the MFI micropores and lower reaction temperatures of around 350 °C.[64] Additionally, isomerisation occurs on weak acid sites while formation of polycyclic aromatics (coke) occurs on strong acid sites, of both Brønsted and Lewis character.[18,19] As the availability of strong acid sites decreases with increased TOS due to coking, the isomerisation products 2,4-dmf, 2-mcpo, and 3-mcpo, are detected as the main products.

The benzene production is quantified and shown in Table 2. In earlier work, a positive correlation between the number of acid sites, i.e., gallium content, and the production of benzene was found for Ga-MFI$_{micro}$.[19] However, for Ga-MFI$_{meso}$, a high gallium content is not needed as most benzene is produced over the G6.7$_{meso}$ (0.776 mmol g^{-1}). Furthermore, production of benzene over the catalyst with the lowest acid site density of 0.052 mmol g^{-1}, G1.2$_{meso}$, was similar to the benzene production over G6.0$_{meso}$, which possesses nearly three times more acid sites (0.140 mmol g^{-1}). This observation suggests that, instead of the acidity, another parameter now plays an important role for the catalytic performance, namely, the secondary pore network including meso- and macropores. Nevertheless, note that the difference in acid sites that are active for benzene formation, might actually be smaller between the two catalysts. To illustrate, a large part of the acid sites of G6.0$_{meso}$ are weak acid sites, as shown in Fig. 6 and S8, which do not catalyse 2,5-dmf aromatization into benzene.

To analyse the effect of the incorporation of mesopores in Ga-MFI zeotypes and the accessibility of the acid sites in more detail, the amount of benzene molecules produced per acid site (benz/site) over the course of three hours reaction was compared, as shown in Table 2. For microporous Ga-MFI, the highest benzene production per site of 4.4 molecules is
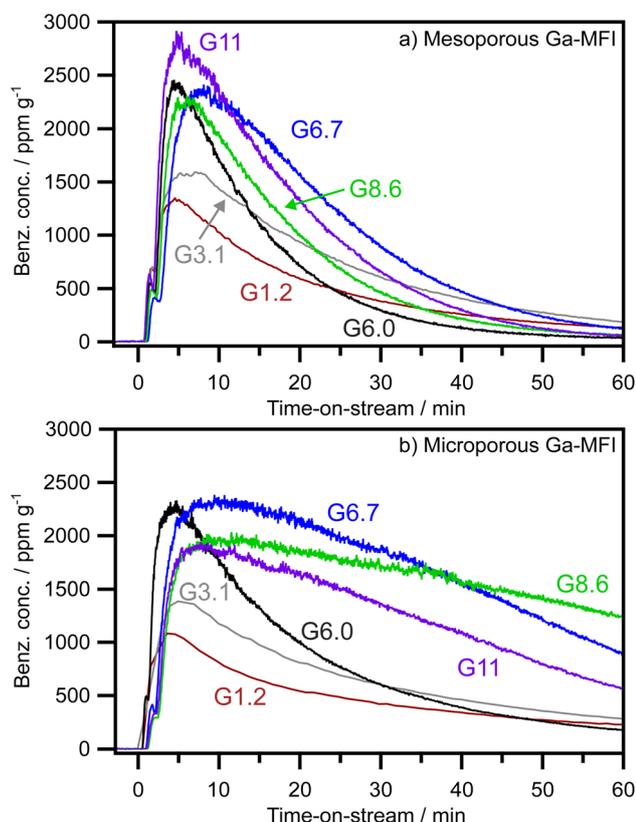
This journal is © The Royal Society of Chemistry 2026

J. Mater. Chem. A, 2026, **14**, 12769–12784 | **12779**

Table 2 Catalytic performance of Ga-MFI$_{meso}$, Ga-MCM-41, Ga-MFI/MCM-41, and Ga-SPP

Sample	WHSV (g_{dmf} g_{cat}^{-1} h^{-1})	Conversion[a] (%)	S_{BTX}[b] (%)	S_{coke}[c] (%)	$C_{balance}$ (%)	Benz. prod[d] (mmol g^{-1})	Benz per site[e]	Benz per site[f]
Ga-MFI$_{meso}$								**Ga-MFI$_{micro}$**
G1.2$_{meso}$	0.42	86.1	64.7	4.2	87.2	0.460	8.8	3.3
G3.1$_{meso}$	0.44	91.3	67.2	7.6	90.2	0.722	5.8	3.3
G6.0$_{meso}$	0.43	91.9	71.6	11.9	92.3	0.501	3.6	2.9
G6.7$_{meso}$	0.44	97.3	82.0	16.3	86.0	0.776	3.1	3.9
G8.6$_{meso}$	0.53	89.5	72.0	14.3	92.9	0.581	2.7	4.4
G11$_{meso}$	0.61	97.4	80.2	15.8	89.3	0.754	2.1	1.9
Ga-MCM-41								
MCM0	0.62	5.3	0.0	N.A.[g]	97.4	0.004[h]	17.9[h]	N.A.
MCM3.1	0.87	33.6	15.7	30.5	97.3	0.064	0.24	N.A.
MCM8.6	0.55	40.3	10.9	26.2	96.8	0.044	0.16	N.A.
MCM8.6-b	0.51	25.7	11.6	31.5	97.3	0.054	0.17	N.A.
MCM11	0.69	23.7	6.9	24.3	96.9	0.030	0.19	N.A.
Ga-MFI/MCM-41								
MFI/MCM0	0.56	3.5	0.0	N.A.[g]	97.9	N.A.	N.A.	N.A.
MFI/MCM3.1	0.63	53.4	32.8	15.4	94.3	0.283	0.92	N.A.
MFI/MCM8.6	1.11	81.6	20.1	35.9	97.7	0.067	0.23	N.A.
MFI/MCM8.6-b	0.59	21.4	14.1	25.7	97.2	0.057	0.17	N.A.
MFI/MCM11	0.69	48.5	14.3	35.7	95.8	0.079	0.25	N.A.
Ga-SPP								
SPP1.2	0.62	9.5	5.3[h]	N.A.[g]	98.3	0.003[h]	4.7[h]	N.A.
SPP2.4	0.39	3.7	20.9[h]	N.A.[g]	96.5	0.002[h]	0.8[h]	N.A.
SPP3.6	0.69	10.8	6.9	38.8	92.5	0.033	4.9[h]	N.A.

[a] Conversion. [b] BTX selectivity at maximum benzene formation. [c] Selectivity towards C_6-equivalent of coke, quantified as CO and CO_2 detected during regeneration. [d] Benzene produced during 3 h 2,5-dmf conversion at 500 °C. [e] Benzene produced per acid site during 3 h reaction. [f] Benzene produced per acid site during 3 h reaction over microporous Ga-MFI.[19] [g] Not available due to low SNR of CO and CO_2 concentrations. [h] Low reliability due to low SNR of ammonia and benzene concentrations.
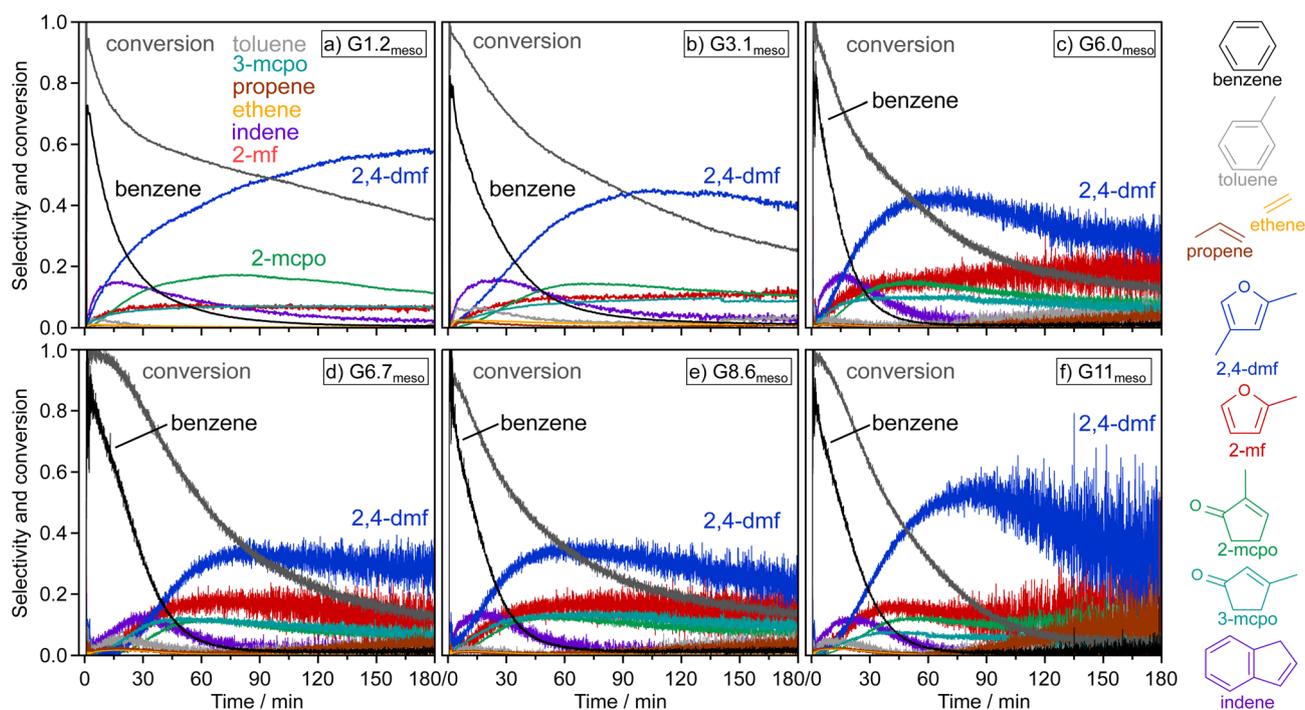

Fig. 9 Catalytic performance of the (a) G1.2$_{meso}$, (b) G3.1$_{meso}$, (c) G6.0$_{meso}$, (d) G6.7$_{meso}$, (e) G8.6$_{meso}$ and (f) G11$_{meso}$ catalysts. Conversion of 2,5-dmf and selectivities of the main products (right side) over mesoporous Ga-MFI zeotypes with 3 h TOS at 500 °C. Concentrations were determined every 15 s (G1.2$_{meso}$ and G3.1$_{meso}$) or every 2 s (other catalysts).

12780 | *J. Mater. Chem. A*, 2026, **14**, 12769–12784

This journal is © The Royal Society of Chemistry 2026

observed for G8.6$_{micro}$, which also produced the most benzene in total. The other microporous catalysts produced, roughly, between three and four molecules of benzene per site, except for G11$_{micro}$ (1.9). The latter suffered from rapid deactivation by coking due to its high acid site density of 0.612 mmol g^{-1}, resulting in an average benzene production of 1.9 molecules per site. After mesopore introduction, benz/site was significantly improved for G1.2$_{meso}$ (8.8) and G3.1$_{meso}$ (5.8), demonstrating a significantly enhanced participation of each acid site to the production of benzene, consequently, an improved accessibility to each acid site. Moreover, the absence of gallium-based nanoparticles in the mesopores of G1.2$_{meso}$ and some of the mesopores of G3.1$_{meso}$ facilitates the mass transport of reactants and products through these pores to the microporous regimes. Smaller increases were observed for G6.0$_{meso}$ (3.6) and G11$_{meso}$ (2.1), while benz/site was decreased for G6.7$_{meso}$ and G8.6$_{meso}$. The reduction in benz/site is likely caused by the loss of acid sites that play a vital role for the production of benzene. By comparing the distributions of the acid sites (Fig. 6 and S8), G6.7$_{meso}$, G8.6$_{meso}$, and G11$_{meso}$ have mainly lost strong Brønsted acid sites while the sBAS fraction was preserved for the other zeotypes. Since sBAS are involved in cracking, decarbonylation, dehydration, and aromatization reactions needed for benzene production, a reduction in the relative number of sBAS results in a reduction in total benzene production in benz/site. The importance of the strong sites is confirmed by NH$_3$-TPD performed on the deactivated catalyst, directly after reaction before regeneration (Fig. 6, black). Here, only weak acid sites with desorption temperatures of <200 °C remain after reaction. However, the negative contribution of a reduced sBAS fraction in G11$_{meso}$ was compensated by a positive contribution caused by its reduced acid site density from 0.612 to 0.354 mmol g^{-1}. This resulted in a lower selectivity to coke (15.8% for G11$_{meso}$ vs. 16.4 for G11$_{micro}$), slower catalyst deactivation and thus an increased catalyst lifetime for benzene production. Combined with the positive contribution of the mesopores, the overall benz/site of mesoporous G11 was higher than microporous G11.

Besides the benzene production per site, the effect of mesopore introduction can be investigated by revisiting the benzene concentrations shown in Fig. 8. Despite the fact that Ga-MFI$_{meso}$ catalysts only possess half of the acid sites as Ga-MFI$_{micro}$, the initial benzene production over Ga-MFI$_{meso}$ (panel a), is higher for each gallium content than Ga-MFI$_{micro}$ (panel b). This suggests a beneficial effect of the introduced mesopores on the mass transport properties, i.e., transport of reactant 2,5-dmf and product benzene at the start of the reaction. However, for each gallium loading, the lifetime of the catalyst in terms of benzene production of Ga-MFI$_{meso}$ is much shorter, implying more rapid catalyst deactivation. One reason for this is their lower number of acid sites, which will be coked faster than a larger number of sites. In combination with its higher initial rate of benzene production, as well as polycyclic aromatic production, this results in a lower catalyst lifetime.

The stability of the short-term reaction over the G6.0$_{meso}$, G6.7$_{meso}$, G8.6$_{meso}$, and G11$_{meso}$ catalysts was tested by an additional four cycles of 3 h 2,5-dmf conversion at 500 °C, and

the conversion and benzene selectivity for all five cycles are shown in Fig. S10. The conversion appears to be stable for all catalysts, suggesting that the structure of the catalysts remains intact. For reference, in a previous study on gallium zeotypes that had been exposed to conditions similar to those present here, XRD and SEM-EDX analyses showed that the structure of the spent zeotype remains primarily unchanged.[19] The acid sites, however, were slightly affected. Here, the benzene selectivity increases slightly in cycle 2 suggesting that acid sites are affected. Thus, the acid sites after the 5th cycle were determined by performing an NH$_3$-TPD, shown in Fig. 6 (grey), and the acid sites were quantified as shown in Table S4. After the consecutive four cycles of reaction, G6.7$_{meso}$, G8.6$_{meso}$, and G11$_{meso}$ have lost some additional acid sites, with 83, 72, and 79% of the initial acid site density remaining. On the contrary, G6.0$_{meso}$, which possessed 101% of the initial acid sites after 1 cycle of reaction, possesses 121% after 5 cycles. The NH$_3$-TPD profiles of regen. 1c (dark blue) show a minor decrease in acid sites that desorb at 290 °C as well as an increase at 410 °C, indicating the mobile nature of the gallium species in the zeotype. During reaction, oxidative regeneration, or even the NH$_3$-TPD temperature ramp itself, additional acid sites can be formed. After five cycles, the increase in extra strong acid sites at 410 °C has grown in size, next to an increase in the weak acid sites, desorbing at 180 °C. This increase in acid site density is not paralleled by an increase in benzene selectivity, Fig. S10, which can be explained twofold. First, the weaker acid sites do not play a major role in benzene production, which is confirmed by the presence of weak acid sites on coked catalysts (Fig. 6, black) even though the catalyst has deactivated completely towards benzene production. Second, the positive effect of the increase in extra strong acid sites may be negated by a deterioration of the micro- and mesoporous network after subsequent cycles of reaction and regeneration. As a result, the first NH$_3$-TPD may have slightly underestimated the acid site density, while after several cycles, these acid sites may have reduced in strength and are thus able to be quantified.

The Ga-MCM-41 and Ga-MFI/MCM-41 catalysts were also evaluated for the conversion of 2,5-dmf, as shown in Fig. S11. For Ga-MCM-41 catalysts, the conversion rapidly decreases to approximately 35% after 30 s of TOS, with main products of indene, benzene, 2-mcpo, and 3-mcpo. From there, the catalyst slowly deactivates to about 20% conversion after three hours of time on stream while mainly producing 3-mcpo, 2-mcpo, and 2-methylfuran. When part of the catalyst has been transformed into MFI, for MFI/MCM3.1, the initial conversion of 2,5-dmf increases to 60% with benzene selectivity reaching 40%. Deactivation occurs but more slowly, with 2,4-dmf becoming the main product after 10 minutes, as was seen for Ga-MFI$_{meso}$. This confirms the necessity of the microporous confinement for isomerisation, as was postulated in previous work.[64]

The total benzene production is quantified and shown in Table 2, typically ranging between 0.030 mmol g^{-1} for MCM11 to 0.067 mmol g^{-1} for MFI/MCM11. An outlier is MFI/MCM3.1, with a production of 0.283 mmol g^{-1}, owing to the confirmed presence of microporous MFI domains that drive the selectivity towards benzene. Even though Ga-MCM-41 catalysts exhibit

This journal is © The Royal Society of Chemistry 2026

J. Mater. Chem. A, 2026, 14, 12769–12784 | 12781

lower benzene production than Ga-MFI$_{meso}$, they typically have higher acid site densities, ranging from 0.161 mmol g^{-1} for MCM11 to 0.349 mmol g^{-1} for MFI/MCM8.6-b. This confirms the hypothesis that acidity is a limiting factor only when MFI-framework is present. The additional high-temperature crystallisation step used for Ga-MFI/MCM-41 resulted in an increase in acid site density, even though it may not have resulted in MFI synthesis for all catalysts. This suggests that even though no transformation into MFI framework was observed for high gallium content catalysts, the additional step may still be beneficial for the crystallisation of amorphous fractions into Ga-MCM-41. For all Ga-MFI/MCM-41 catalysts, the slight increase in acid site density matches an increase in benzene production. This suggests that increasing the benzene production within one type of framework, MCM-41, can be improved by increasing the acid site density.

The bigger dimensions of the mesopores also allow for the formation of larger polyaromatic hydrocarbons and other coke precursors, such as indene. For MCM3.1, MCM8.6, MFI/MCM8.6, and MFI/MCM11, the main product at the start of the reaction is indene instead of benzene or one of the isomerisation products 2-mcpo and 3-mcpo. Additionally, the coke selectivity typically ranges between 25 and 35%, much higher than what was observed for Ga-MFI$_{meso}$. However, the coke selectivity might become inflated if the catalyst rapidly deactivates to all reactions, as it depends on the concentrations of all measured products. A fairer metric would be the amount of coke-C$_6$ equivalents detected per benzene (not shown), which yields a similar trend of an increased coke formation on Ga-MCM-41 and Ga-MFI/MCM-41. One exception is MFI/MCM3.1, the micro- and mesoporous composite which has a coke selectivity of 15.4%, nearly half of its fully mesoporous MCM3.1 analog. This demonstrates the importance of the presence of micropores to drive the reaction towards monoaromatics like benzene and thus suppress the formation of coke.

The Ga-SPP catalysts were also evaluated for the conversion of 2,5-dmf but were nearly inactive, producing 0.003, 0.002, and 0.033 mmol g^{-1} benzene for SPP1.2, SPP2.4, and SPP3.6, respectively (Table 2). Due to the low conversion of 2,5-dmf, the SNR of the detected species is low which increases the error in the determined acidity, benzene production, and benz/site of the catalysts. The detected product concentrations, not the selectivities, are shown in Fig. S12. The main products are water, CO, and CO$_2$, indicating the presence of decarbonylation and dehydration reactions. For SPP3.6, some products are detected in minor concentrations, up to 2 ppm, such as benzene, toluene, propene, and 2-mcpo. However, the selectivity towards coke was determined to be 38.8%, suggesting that the larger mesopores of Ga-SPP favour the production of coke over benzene.

In summary, this work has investigated three different approaches for introducing mesoporosity in microporous catalysts and its influence on the conversion of 2,5-dmf into monocyclic aromatics, foremost benzene. The methods include (i) a top-down dissolution–recrystallisation procedure to create a secondary pore network of meso- and macropores in pre-synthesised microporous Ga-MFI to achieve a hierarchical Ga-MFI zeotype, (ii) a bottom-up synthesis of Ga-containing MFI/MCM-41 composites, in which first a mesoporous MCM-41 framework was synthesised followed by hydrothermal crystallisation to convert parts of the mesopore walls into microporous MFI and (iii) synthesis of Ga-containing self-assembled pillared pentasil (Ga-SPP) units with intercrystalline meso- and macropores originating from randomly ordered regions of microporous MFI. The introduction of mesopores affects several parameters important for the catalytic activity and the lifetime of the catalyst such as specific surface area and mesoporous volume, acid site density and strength, and accessibility of reactants to the catalytic sites. For low gallium content hierarchical Ga-MFI$_{meso}$ zeotypes, an increase in mesoporous volume corresponds to a decrease in total surface area, while for higher gallium content zeotypes, the removal of gallium-based nanoparticles resulted in an increase in both surface area and microporous volume. Approximately half of the acid sites were lost during mesopore introduction; primarily weak Lewis acid sites for low gallium content zeotypes, while high gallium content zeotypes lost mainly strong Brønsted acid sites. As a result, the total benzene production and benzene production per acid site decrease for G6.7$_{meso}$ and G8.6$_{meso}$, while the benzene production per site increases for all other zeotypes. This confirms the advantageous effect of incorporating mesopores into microporous Ga-MFI zeotypes. Additionally, the enhanced mass transport results in a higher initial benzene production for hierarchical Ga-MFI for all gallium contents. Gallium-doped mesoporous silica, Ga-MCM-41, possesses higher acid site densities than Ga-MFI$_{meso}$, but the production of benzene is much lower because the selectivity towards coke precursors like indene and coke is higher. Despite having similar acid site density, the Ga-MFI/MCM-41 composite with a gallium content of 3.1 wt% demonstrates a much higher production of benzene and consequently lower selectivity to coke than its Ga-MCM-41 analog, which evidences that the presence of a microporous MFI-framework is vital to drive the selectivity of the reaction towards monocyclic aromatics like benzene. Additionally, implementing micropores into an existing mesoporous structure results in a lower benzene production than implementing mesopores into a microporous structure, like done for Ga-MFI$_{meso}$, regardless of its acid site density. The gallium-doped self-assembled pentasil units possess a wide range of mesopores with fractions of microporous MFI, but their acidity is nearly zero and thus practically inactive for the production of aromatics (displaying some activity towards the production of coke). This series demonstrates that the combination of both micro- and mesopores is beneficial for the benzene production only if a critical acid site density is reached.

4 Conclusion

For Ga-zeotypes, microporosity is shown to be required to drive the conversion of 2,5-dmf toward monocyclic products such as benzene. However, site accessibility is limiting the catalytic efficiency and thus hierarchical Ga-MFI zeotypes show higher initial benzene production independent of Ga content as compared to their microporous counterparts. As a function of

12782 | J. Mater. Chem. A, 2026, 14, 12769–12784

This journal is © The Royal Society of Chemistry 2026

time on stream, the total benzene production depends on the evolution of strong Brønsted acid sites. Hence, for Ga-MFI$_{meso}$ zeotypes with low Ga content, the total benzene production and the benzene produced per acid site increase as compared to microporous counterparts, whereas for G6.7$_{meso}$ and G8.6$_{meso}$ the opposite is observed. Besides, introducing a too high fraction of mesopores in combination with significant acid site density risks to change the product selectivity towards coke precursors and eventually coke. Thus, designing the optimal hierarchical Ga-MFI zeotype is shown to be a delicate balancing act where specific surface area, mesoporous volume, acid site strength and density, all need to be weighed together and tested for the target reaction at hand.

Author contributions

Guido J. L. de Reijer: conceptualization, investigation, writing – original draft. Andreas Schaefer: supervision, writing – review & editing. Anders Hellman: supervision, writing – review & editing. Per-Anders Carlsson: supervision, funding acquisition, writing – review & editing.

Conflicts of interest

There are no conflicts to declare.

Data availability

The data supporting this article have been included as part of the supplementary information (SI). Supplementary information: catalyst synthesis; flow reactor setup; procedures for catalytic tests and NH$_3$-TPD; procedure for pyridine DRIFTS; conversion and selectivity; elemental composition; structural characterisation; catalytic performance tests and long-term stability. See DOI: https://doi.org/10.1039/d5ta09751g.

Acknowledgements

Notes and references

1 ACC, *Guide to the Business of Chemistry*, American Chemistry Council, 2020.

2 R. W. Thring, S. P. Katikaneni and N. N. Bakhshi, *Fuel Process. Technol.*, 2000, **62**, 17–30.

3 J. Tickner, K. Geiser and S. Baima, *Environment*, 2021, **63**, 4–15.

4 R. Bielski and G. Grynkiewicz, *Green Chem.*, 2021, **23**, 7458–7487.

5 F. A. Kucherov, L. V. Romashov, G. M. Averochkin and V. P. Ananikov, *ACS Sustainable Chem. Eng.*, 2021, **9**, 3011–3042.

6 W. H. Gong, *Recent Perspectives in Pyrolysis Research*, IntechOpen, 2022.

7 A. Al Ghatta and J. P. Hallett, *RSC Sustainability*, 2023, **1**, 698–745.

8 J. Gancedo, L. Faba and S. Ordonez, *ACS Sustain. Chem. Eng.*, 2022, **10**, 7752–7758.

9 M. Cook and W. Conner, *Proceedings of the 12th International Zeolite Conference*, Warrendale, 1999.

10 J. Jae, G. A. Tompsett, A. J. Foster, K. D. Hammond, S. M. Auerbach, R. F. Lobo and G. W. Huber, *J. Catal.*, 2011, **279**, 257–268.

11 R. Szostak, *Molecular Sieves—Principles of Synthesis and Identification*, 1989, vol. 213, p. 325.

12 C. D. Baertsch, H. H. Funke, J. L. Falconer and R. D. Noble, *J. Phys. Chem.*, 1996, **100**, 7676–7679.

13 A. J. Foster, J. Jae, Y.-T. T. Cheng, G. W. Huber and R. F. Lobo, *Appl. Catal., A*, 2012, **423–424**, 154–161.

14 Y. Fang, F. Yang, X. He and X. Zhu, *Front. Chem. Sci. Eng.*, 2019, **13**, 543–553.

15 M. Seifert, M. S. Marschall, T. Gille, C. Jonscher, O. Busse, S. Paasch, E. Brunner, W. Reschetilowski and J. J. Weigand, *ChemCatChem*, 2020, **12**, 6301–6310.

16 S. Creci, X. Wang, P.-A. Carlsson and M. Skoglundh, *Top. Catal.*, 2019, **62**, 689–698.

17 S. Creci, A. Martinelli, S. Vavra, P.-A. Carlsson and M. Skoglundh, *Catalysts*, 2021, **11**, 1–12.

18 C. Sauer, G. J. L. de Reijer, A. Schaefer and P.-A. Carlsson, *Top. Catal.*, 2023, **66**, 1329–1340.

19 G. J. de Reijer, A. Schaefer, A. Hellman and P. A. Carlsson, *Ind. Eng. Chem. Res.*, 2025, **64**, 2025–2035.

20 C. Torri, I. G. Lesci and D. Fabbri, *J. Anal. Appl. Pyrolysis*, 2009, **85**, 192–196.

21 F. W. Yu, D. X. Ji, Y. Nie, Y. Luo, C. J. Huang and J. B. Ji, *Appl. Biochem. Biotechnol.*, 2012, **168**, 174–182.

22 M. J. Jeon, J. K. Jeon, D. J. Suh, S. H. Park, Y. J. Sa, S. H. Joo and Y. K. Park, *Catal. Today*, 2013, **204**, 170–178.

23 A. Toledano, L. Serrano, A. Pineda, A. A. Romero, R. Luque and J. Labidi, *Appl. Catal., B*, 2014, **145**, 43–55.

24 Y. K. Park, M. L. Yoo and S. H. Park, *J. Nanomater.*, 2014, **596584**, 5.

25 S. Kasipandi, J. M. Cho, K. S. Park, C. H. Shin and J. Wook Bae, *J. Catal.*, 2020, **385**, 10–20.

26 F. Shi, J. Wang, H. Wang, C. Liu, Y. Lu, X. Lin, D. Hou, C. Wen, S. Yang, C. Luo, Z. Zheng and Y. Zheng, *J. Energy Inst.*, 2023, **108**, 101206.

27 V. R. Elías, G. O. Ferrero, M. G. Idriceanu, G. A. Eimer and M. E. Domine, *Catal.:Sci. Technol.*, 2024, **14**, 1488–1500.

28 T. Sun, L. Zhang, Y. Yang, Y. Li, S. Ren, L. Dong and T. Lei, *Int. J. Environ. Res. Publ. Health*, 2022, **19**, 16837.

29 M. M. Antunes, K. Skrodczky, P. S. Cabanelas, N. Pinna, P. A. Russo and A. A. Valente, *Green Chem.*, 2024, **26**, 4820–4833.

30 S. Mardiana, N. J. Azhari, T. Ilmi and G. T. Kadja, *Fuel*, 2022, **309**, 122119.

This journal is © The Royal Society of Chemistry 2026

J. Mater. Chem. A, 2026, **14**, 12769–12784 | **12783**

31 R. Li, D. Huang, Z. Wei, Y. Chen, G. Wang, W. Zhou, R. Xiao and W. Xu, *Renew. Sustain. Energy Rev.*, 2025, **207**, 114977.

32 S. Liu, Z. Cheng, B. Li, H. Zeng, W. Liang, Y. Luo, Y. Bai, H. Gao, X. Pan and X. Shu, *Mater. Today Sustain.*, 2024, **27**, 100917.

33 S. Soltanian, C. L. Lee and S. S. Lam, *Biofuel Res. J.*, 2020, **7**, 1217–1234.

34 T. W. Kim, S. Y. Kim, J. C. Kim, Y. Kim, R. Ryoo and C. U. Kim, *Appl. Catal., B*, 2016, **185**, 100–109.

35 S. C. Vasconcelos, V. Rossa, D. G. Quattrociocchi, V. G. Madriaga, M. C. O. Ribeiro, S. B. Pinheiro, R. D. d. Santos, B. S. Archanjo, E. A. Urquieta-González, A. V. Soares, *et al.*, *Energy Fuels*, 2024, **38**, 23823–23835.

36 L. Pinard, L. Jia, N. Pichot, A. Astafan and A. Dufour, *Energy Fuels*, 2024, **38**, 14351–14364.

37 W. Zhang, B. Wang, P. Rui, N. Fan and W. Liao, *Catal. Lett.*, 2021, **151**, 2716–2723.

38 Q. Zhang, Y. Zhai, F. Wang, X. Zhang, G. Lv, Y. Liu, M. Li and M. Li, *Microporous Mesoporous Mater.*, 2022, **329**, 111515.

39 W. G. Kim, J. So, S. W. Choi, Y. Liu, R. S. Dixit, C. Sievers, D. S. Sholl, S. Nair and C. W. Jones, *Chem. Mater.*, 2017, **29**, 7213–7222.

40 S. Brunauer, P. H. Emmett and E. Teller, *J. Am. Chem. Soc.*, 1938, **60**, 309–319.

41 J. Rouquerol, P. Llewellyn and F. Rouquerol, *Stud. Surf. Sci. Catal.*, 2007, **160**, 49–56.

42 G. Jura and W. D. Harkins, *J. Am. Chem. Soc.*, 1944, **66**, 1356–1362.

43 A. Galarneau, F. Villemot, J. Rodriguez, F. Fajula and B. Coasne, *Langmuir*, 2014, **30**, 13266–13274.

44 E. P. Barrett, L. G. Joyner and P. P. Halenda, *J. Am. Chem. Soc.*, 1951, **73**, 373–380.

45 C. Sauer, A. Lorén, A. Schaefer and P.-A. Carlsson, *Anal. Chem.*, 2021, **93**, 13187–13195.

46 C. Sauer, A. Lorén, A. Schaefer and P.-A. Carlsson, *Catal.:Sci. Technol.*, 2022, **12**, 750–761.

47 M. Inui, T. Ikeda, T. Suzuki, K. Sugita and F. Mizukamil, *Bull. Chem. Soc. Jpn.*, 2009, **82**, 1160–1169.

48 M. J. Costa, T. Chellappa, A. S. Araujo, V. M. Fonseca, V. J. Fernandes, R. M. Nascimento and J. G. Pacheco, *Aust. J. Chem.*, 2014, **68**, 99–105.

49 H. Kosslick, V. A. Tuan, B. Parlitz, R. Fricke, C. Peuker and W. Storek, *J. Chem. Soc., Faraday Trans.*, 1993, **89**, 1131–1138.

50 M. Thommes, K. Kaneko, A. V. Neimark, J. P. Olivier, F. Rodriguez-Reinoso, J. Rouquerol and K. S. Sing, *Pure Appl. Chem.*, 2015, **87**, 1051–1069.

51 J. C. Groen, L. A. Peffer and J. Pérez-Ramírez, *Microporous Mesoporous Mater.*, 2003, **60**, 1–17.

52 P. L. Llewellyn, J. P. Coulomb, Y. Grillet, J. Patarin, G. Andre and J. Rouquerol, *Langmuir*, 1993, **9**, 1852–1856.

53 U. Müller and K. K. Unger, *Stud. Surf. Sci. Catal.*, 1988, **39**, 101–108.

54 U. Müller, H. Reichert, E. Robens, K. K. Unger, Y. Grillet, F. Rouquerol, J. Rouquerol, D. Pan and A. Mersmann, *Fresenius' Z. für Anal. Chem.*, 1989, **333**, 433–436.

55 H. Reichert, U. Müller, K. K. Unger, Y. Grillet, F. Rouquerol, J. Rouquerol and J. P. Coulomb, *Stud. Surf. Sci. Catal.*, 1991, **62**, 535–542.

56 F. Rouquerol, J. Rouquerol, K. Sing, P. Llewellyn and G. Maurin, *Adsorption by Powders and Porous Solids: Principles, Methodology and Applications*, Academic Press, 2014, pp. 505–506.

57 S. Gregg and K. Sing, *Adsorption, Surface Area and Porosity*, Academic Press Inc., New York, ed. 2nd, 1982.

58 K. S. Sing and R. T. Williams, *Adsorpt. Sci. Technol.*, 2004, **22**, 773–782.

59 J. Čejka, A. Corma and S. Zones, *Zeolites and Catalysis, Synthesis, Reactions and Applications*, Wiley-VCH, 2010, pp. 136–137.

60 Y.-T. Cheng and G. W. Huber, *Green Chem.*, 2012, **14**, 3114–3125.

61 E. A. Uslamin, B. Luna-Murillo, N. Kosinov, P. C. Bruijnincx, E. A. Pidko, B. M. Weckhuysen and E. J. Hensen, *Chem. Eng. Sci.*, 2019, **198**, 305–316.

62 Y. Sun, L. Wei, Z. Zhang, H. Zhang and Y. Li, *Energy Fuels*, 2023, **37**, 1657–1677.

63 C. Wang-Hansen, C. J. Kamp, M. Skoglundh, B. Andersson and P.-A. Carlsson, *J. Phys. Chem. C*, 2011, **115**, 16098–16108.

64 C. Sauer, G. J. L. de Reijer, B. Wilfinger, A. Hellman and P.-A. Carlsson, *Chem.–Eur. J.*, 2024, **30**, e202303810.

12784 | *J. Mater. Chem. A*, 2026, **14**, 12769–12784

This journal is © The Royal Society of Chemistry 2026